Rapid Communications

Quantifying Jahn-Teller distortion at the nanoscale with picometer accuracy using position averaged convergent beam electron diffraction

Binbin Wang,[1,2] Bryan D. Esser,[2] Núria Bagués,[2] Robert E. A. Williams,[2] Jiaqiang Yan,[3] and David W. McComb[1,2,*]

[1]*Department of Materials Science and Engineering, The Ohio State University, Ohio 43210, USA*

[2]*Center for Electron Microscopy and Analysis, The Ohio State University, Ohio 43212, USA*

[3]*Materials Science and Technology Division, Oak Ridge National Laboratory, Tennessee 37831, USA*

(Received 29 July 2019; published 12 December 2019)

Using position averaged convergent beam electron diffraction (PACBED) the Jahn-Teller distortion in $LaMnO_3$ is quantitatively measured using a straightforward pattern-matching approach. The fit between experimental patterns and PACBED patterns simulated using the quantum excitation of phonons model allows a three-dimensional measure of octahedral distortion and rotation information from the near transmitted disk region with picometer precision. The effects of plasmon and other inelastic components on quantification using this method are investigated and discussed. The results provide an avenue for accurate local studies of the crystal structure origins of emergent physics in parallel with high-resolution annular dark field scanning transmission electron microscopy imaging at interfaces and defects in quantum materials.

DOI: 10.1103/PhysRevResearch.1.032037

In AMO_3 perovskites with *Pbnm* space group, cooperative octahedral, $MO_{6/2}$ site rotations are accompanied by universal, intrinsic site distortions that fundamentally influence electronic and magnetic properties [1–3]. For example, some transition metal ions (i.e., Cu^{2+} and Mn^{3+}) on the octahedral site exhibit cooperative Jahn-Teller distortions (JTDs) that can result in a range of fascinating phenomena including charge, spin, and orbital ordering [1,4]. Although direct imaging of these physical properties is challenging, they can be accurately inferred via indirect measurements of octahedral distortion [5–7].

While there are some reports of experimental measurements of octahedral bonding parameters in perovskites using neutron diffraction and resonant x-ray scattering techniques [5,8,9], these techniques have limited spatial resolution, making them ill suited for characterizing local properties at interfaces and other defects [2,10,11]. In contrast, aberration-corrected scanning transmission electron microscopy (STEM) is extensively used for its ability to probe local phenomena [12,13]. However, quantifying octahedral distortions in real-space STEM images is challenging because it requires a precise measurement of the projected positions of cations and anions (oxygen, in this case). Since oxygen (O) has a relatively weak scattering cross section compared to typical cations in perovskites, techniques such as annular bright field imaging, electron energy-loss spectroscopy, and differential phase contrast imaging are often used to directly image the O columns [14–16]. While postprocessing can allow octahedral rotation types to be deduced in specific cases [17–20], picometer-scale distortions in the anion octahedron and cation positions, as well as three-dimensional (3D) octahedral rotations are typically beyond the spatial resolution of even the most advanced STEM instruments [21–23]. Moreover, postprocessing artifacts and image distortion caused by probe instabilities and/or specimen drift can further complicate the situation.

Quantitative convergent beam electron diffraction (CBED) is a complementary diffraction-based technique capable of high-precision nanoscale measurements. This technique has been used in a broad number of applications over the past few decades, such as determining thickness [24], crystal structural parameters [25], bonding [26,27], and Debye-Waller factors [28]. However, the electron optical and diffraction conditions in these applications make it difficult to obtain a large data set of high-resolution images, especially atomic resolution imaging with a thin specimen [29]. Instead, position averaged convergent beam electron diffraction (PACBED) has recently been developed in which the patterns can be recorded in parallel with high-resolution STEM images without the need to change optical conditions [30,31]. Moreover, PACBED is independent of coherent and incoherent aberrations such as defocus and spherical aberration [29]. By incoherently averaging diffraction patterns formed by rastering an atomic-scale probe across one or more unit cells, a wealth of information is encoded in the intensity distribution around the zero-order disk. By pattern-matching algorithms, PACBED has been used to investigate specimen properties such as thickness [32,33], tilting of octahedra [29], and polarization [34]. In this article, single-crystal $LaMnO_3$ is selected to investigate intensity distribution changes in PACBED patterns caused by JTD, and the resultant structural parameters are compared with results from multiple complementary methods

*mccomb.29@osu.edu

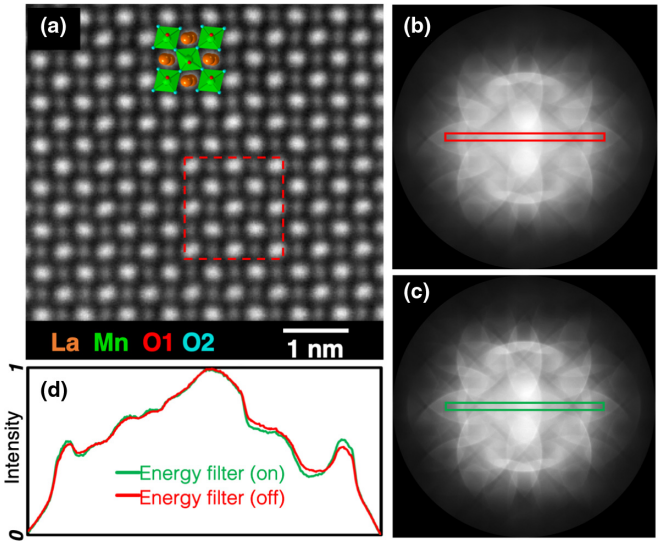

FIG. 1. Experimental STEM image and PACBED patterns. (a) HAADF-STEM image for $LaMnO_3$ along the [001] direction with an overlay of the lattice. Nonlinear drift distortion is corrected using image pairs with orthogonal scan directions [20]. PACBED patterns acquired from the area indicated by the red dashed box in (a) with energy filter off (b) and energy filter on (c). Normalized intensity integration along the red and green boxes is shown in (d) to highlight differences between the two images. The asymmetry along the intensity profile is likely caused by a slight deviation of the sample from the exact zone axis. The transmitted disk size is 9.7 mrad.

[5,8,35]. It will be demonstrated that the JTD of octahedra in $LaMnO_3$ can be quantitatively measured by matching PACBED patterns in experimental and simulated PACBED patterns. The measured JTD and octahedral tilts in $LaMnO_3$ agree with published structural parameters found by other techniques within picometer uncertainty. We also demonstrate improved reliability by filtering the inelastic components of the diffraction patterns using a postspecimen energy filter.

Single crystals of $LaMnO_3$ were grown by the floating zone technique and TEM specimens were prepared using a FEI Helios NanoLab 600 DualBeam focused ion beam (FIB) with 30-kV Ga ions. Final cleaning passes were performed in a Fischione NanoMill with 900-V and then 500-V Ar ions to remove any potential amorphous surface damage created in the FIB. High-angle annular dark field (HAADF) STEM imaging was performed along the [001] direction on a probe aberration-corrected FEI Titan 80–300 STEM at 300 kV with a collection range of approximately 45–293 mrad, as shown in Fig. 1(a). Since HAADF-STEM imaging provides Z contrast, La columns exhibit the highest intensity, while the lighter Mn columns are less intense. Contrast on the La columns is indicative of the projection of displaced La atoms and helps to identify the in-plane orientation of the crystal. PACBED was acquired at the 2×2 unit cell with 9.7-mrad convergence semiangle (α) as indicated by the red dashed box in Fig. 1(a). A Gatan Imaging Filter and Gatan 969 K2 direct electron detector (1024×1024 pixels) were used to acquire energy filtered PACBED with 10-s integration time and a 10-eV energy slit centered on the zero-loss beam, while the unfiltered images were acquired under the same conditions without the energy slit. The lattice parameter was measured at room temperature by fitting the diffracted disks in the PACBED pattern. By comparing the experimental pattern to simulated ones, the thickness of the specimen in the electron beam direction was measured to be 31.0 ± 0.7 nm using the PACBED shown in Fig. 1(b) [32]. A slight specimen tilt of 0.5 mrad is observed and measured using the distance between the whole pattern center of mass and the center of the transmitted disk.

Electron diffraction and by extension STEM imaging can be numerically derived [36,37]. To understand the contribution of octahedral distortions in Figs. 1(b) and 1(c), PACBED patterns were simulated using the quantum excitation of phonons (QEP) model in μSTEM, where thermal scattering is treated as a quantum excitation of the crystal [38]. In the QEP model, the probability distribution for a single electron is solved based on many-body quantum mechanics, and the measurement is modeled as the incoherent sum of the electrons that scattered from different initial states [36]. In practical terms, the crystal is modeled as independent harmonic oscillators, where each atom's distribution can be described by its Debye-Waller factors. In this work, the Debye-Waller factor values are obtained from Ref. [39]. Fully quantitative interpretation of PACBED can be challenging as the patterns include interference between the elastic and inelastic scattering contribution, as well as thickness-dependent, collective excitations which include channeling, thermal scattering, plasmons, and ionization scattering. The last two factors can be overcome experimentally by imaging with an energy filter. Figure 1(d) shows a comparison of the aligned contrast profile of PACBED patterns with and without energy filter under the same acquisition conditions. The energy filtered PACBED shows more details in the transmitted disk than the unfiltered one in which electrons have undergone greater energy losses, obscuring the purely elastic scattering contribution. Since no collective excitations are involved in the simulation, it is helpful to use an energy filter to remove the inelastic background for reliable quantification of the experimental measurement.

In order to understand the intensity contrast in experimental PACBED, QEP simulations were performed with a systematic series of crystal structures with varying combinations of octahedral rotations and bond distance factors. To speed up the fitting process, we used a coarse-to-fine strategy in our simulations such that different space groups and large parameter range are explored in the preparation "coarse" work for identifying the prototype crystal structure model. After that, according to the results, $LaMnO_3$ was restricted to an orthorhombic symmetry (*Pbnm*) which shows in-phase octahedral tilting along the c axis, while the out-of-phase octahedral tilting is in the ab plane [Fig. 2(a)]. Additionally, Mn atoms were made to remain centered within their respective octahedra. Each octahedron consists of two types of oxygen (O1 and O2), where Mn-O2 is the cooperative JTD active bonds, i.e., two short and two long bonds, as shown in Fig. 2(a). With these restrictions, the set of crystal structures was generated from two sets of variables: the magnitude of the octahedral tilting (δ and γ) and the bond distances ratio, J [Mn-O2 (short)/Mn-O2(long)]. Here we define δ as the magnitude of rotation about the [001] direction, and γ as the

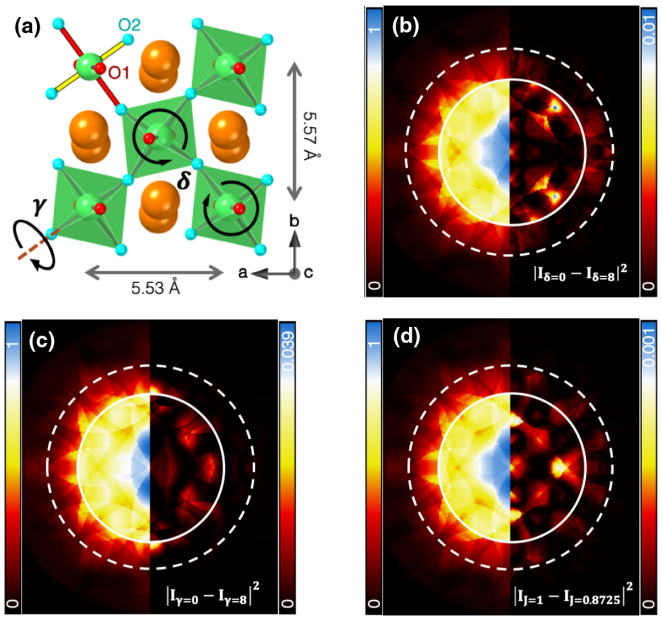

FIG. 2. Intensity variation in PACBED with varying octahedral parameters. (a) Crystal structure of $LaMnO_3$. PACBED (left) and the squared difference between the perfect structure and the distorted one (right) as a function of (b) δ-type rotation, (c) γ -type rotation, and (d) bonding ratio. The white solid and dashed circles indicate the transmitted disk (1α) and 1.4α, respectively. The intensity in each pattern is normalized to show the contrast detail and its scale is arbitrary.

rotation about [110]. Mn-O2 is on the JTD active plane (001) while the Mn-O1 is along the perpendicular direction.

In Fig. 2, we show the simulated PACBED patterns as a function of octahedral rotation and distortion using imaging conditions consistent with the experimental parameters. Figure 2 shows PACBED patterns are sensitive to changes in each variable (δ, γ, and J). The perfect crystal has no octahedral rotation ($\delta = \gamma = 0$) and no active JTD ($J = 1$); the intensity difference of the PACBED patterns between perfect crystal structure and the prototype crystal structure with octahedral rotation ($\delta = \gamma = 0$) and active JTD ($J = 0.8725$) is squared and normalized [Figs. 2(b)–2(d)]. The majority of the change in scattering occurs at low scattering angles ($<\alpha$) within the overlap between the transmitted and diffracted disks, while barely any difference in the signals can be observed beyond 1.4α, as indicated by the dashed circles in Figs. 2(b)–2(d)]. Therefore, scattering angles were limited to 1.4α in the following analysis to reduce background noise.

To quantify agreement between experimental and simulated PACBED patterns, all patterns are masked such that all intensity at angles greater than 1.4α is set to 0, while scattering less than 1.4α is normalized on a [0,1] scale. Additionally, experimental PACBED images are down-sampled to the same number of pixels as the simulated patterns. The best fit is defined by a nonlinear least-squares fitting parameter χ^2 [40,41]:

$$\chi^2 = \frac{1}{N_{\text{pixel}}} \sum_{i,j} [\mathrm{I}_{\text{expt}}(x_i, y_j) - I_{\text{sim}}(x_i, y_j)]^2,$$

where the lowest average squared difference between the intensity of the experimental I_{expt} and the simulated I_{sim} patterns represents the best fit.

In Fig. 3(a), the minimum of χ^2 indicates the best agreement between experimental energy filtered PACBED [shown in Fig. 1(b)] and simulated patterns of structures with varying octahedral rotation and a fixed Mn-O2(short)/Mn-O2(long) ratio. Because octahedral rotation and bonding ratio can both contribute to octahedral distortion, the magnitude of the octahedral distortion that relates to each minimum χ^2 value is

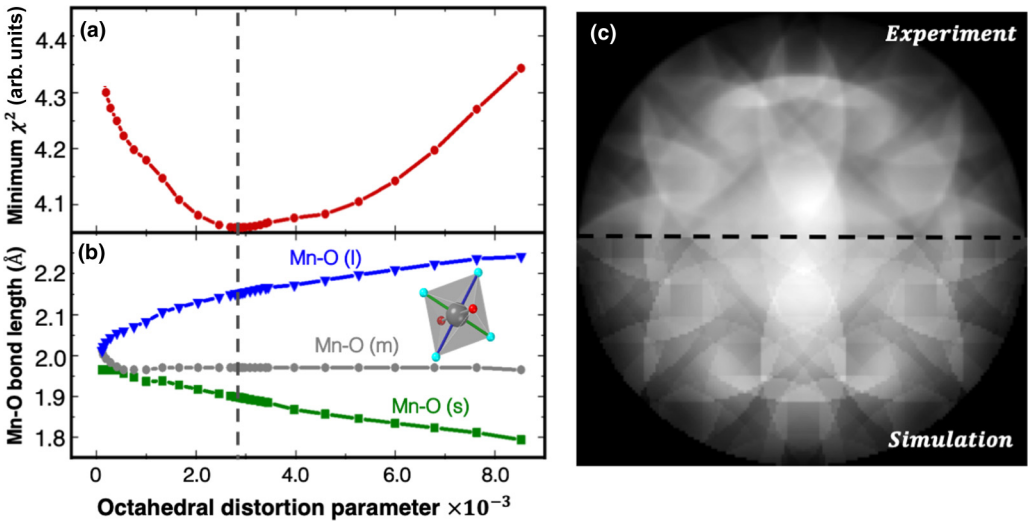

FIG. 3. Comparison between experimental energy filtered PACBED and simulated patterns as a function of the simulated octahedral distortion parameter. (a) Minimum χ^2 in the permutation of δ and γ type octahedral distortions ($0^\circ - 15^\circ$) with fixed bonding ratio J (0.7–1). The Mn-O bond lengths (b) correspond to the simulated structure of each minimum χ^2 in (a). Comparison between the down-sampled pattern and simulated pattern that determined the best fitting parameters in (c). The measurement steps are controlled by following a rough-to-fine strategy. The gray dashed line in these figures shows the position of the best fit condition.

TABLE I. Octahedral parameters measured from PACBED reconstructed structure compared with corresponding neutron diffraction (ND), resonant x-ray scattering (RXS), and density-functional theory (DFT) results at room temperature.

Method	Ref [5]. ND	Ref. [8] RXS	Ref. [35] DFT+U	Expt. PACBED
Mn-O(l) (Å)	2.178 ± 0.001	2.19 ± 0.03	2.168	2.14 ± 0.02
Mn-O(m) (Å)	1.968 ± 0.003		1.974	1.97 ± 0.02
Mn-O(s) (Å)	1.907 ± 0.001	1.92 ± 0.01	1.927	1.89 ± 0.02
Mn-O(s)/Mn-O(l)	0.875 ± 0.001	0.87 ± 0.01	0.889	0.88 ± 0.01
$\Delta d(\times 10^{-3})$	3.31		2.67	2.89
$\theta 1$ = Mn-O1-Mn	155.45 ± 0.02		153.5	156.1 ± 0.5
$\theta 2$ = Mn-O2-Mn	154.97 ± 0.05		152.2	153.6 ± 1.0

quantified by the octahedral distortion parameter Δd [42]:

$$\Delta d = \frac{1}{6} \sum_{n=1,6} \left[\frac{(d_n - \bar{d})}{\bar{d}} \right]^2,$$

where $\bar{d}$ is the mean Mn-O bond distance; d_n are the individual Mn-O bond distances. The corresponding Mn-O bond distances for each datum are shown in Fig. 3(b).

There is a clear and unambiguous minimum χ^2 as a function of Δd in Fig. 3(a). The best fit appears when Δd is $(2.89 \pm 0.1) \times 10^{-3}$. The corresponding Mn-O bond lengths are 2.14 ± 0.02 Å, 1.97 ± 0.02 Å, and 1.89 ± 0.02 Å. The step size for octahedral rotations in these simulations was set to be 0.5° due to computational demands, which leads to the uncertainty in bond distances of approximately 0.02 Å. Since the uncertainties of bond distances are calculated using the upper bounds of the step sizes, the actual uncertainty might be lower. Although smaller steps would improve the precision, a 0.5° step size is acceptable in this case considering the magnitude of the distortion in $LaMnO_3$ (~0.27 Å).

To further check the accuracy of the PACBED derived structure, in Table I we present experimentally measured and theoretically calculated crystal parameters of bulk $LaMnO_3$ at room temperature together with our results [5,8,35]. In terms of Mn-O bonding distances, the PACBED results are consistent with the neutron diffraction results within a few picometers, which may come from surface reconstruction and relaxation due to the finite size of the TEM specimen.

Here it is necessary to highlight the influence of inelastic scattering in PACBED quantification because collective excitations are not included in the simulation, such as surface plasmons. In Fig. 4 we show the effect of inelastic scattering in PACBED on the accuracy of octahedral distortion parameter measurements. Compared to energy filtered patterns, the sensitivity of Δd measurements using unfiltered pattern decreases and the best fit Δd is shifted about 1.2×10^{-3} from the energy filtered result.

In practice, the ability to acquire energy filtered PACBED is instrument dependent. To ameliorate the effect of inelastic components in a typical unfiltered PACBED pattern, one can postprocess the pattern with a background subtraction where background images are produced from the original unfiltered PACBED patterns using a two-dimensional (2D) Gaussian blur. The resultant background subtracted image is the normalized net difference between the original and background image. An empirical Gaussian blur radius is the diameter of the transmitted disk (2α). As shown in Fig. 4, when the radius is set to be 2α, the measured Δd is close to the result from the energy filtered pattern. The arbitrary choice of a Gaussian blur, however, may introduce random error in the background removal process. In this case, if the blur radius decreases to the radius of the transmitted disk (1α), the measured Δd starts to diverge from the expected result. While energy filtering is the preferred method when available, such background subtraction is useful in combatting certain inelastic effects that cannot easily be simulated.

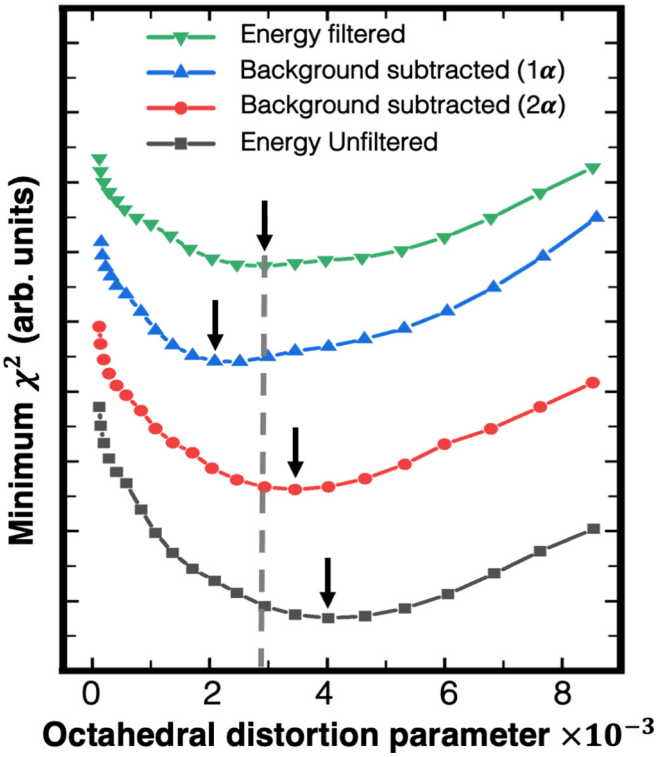

FIG. 4. The effect of inelastic scattering on the measurement of the octahedral distortion parameter and its amelioration by removing a background. Black squares are the measurement using the original unfiltered PACBED pattern. Then different background is produced using Gaussian blur to remove from the original pattern 2α Gaussian blur radius for red circle line and 1α Gaussian blur radius for green triangle line. Black arrows indicate the best fit result for each measurement, while the gray dashed line marks the result measured from energy filtered PACBED.

In summary, we have demonstrated that Jahn-Teller distortions in $LaMnO_3$ can be quantitatively measured with picometer precision at the nanometer scale using the near-transmitted disk region of PACBED. The measurement of Mn-O bonding distances is consistent with neutron diffraction results with an accuracy of approximately 0.02 Å. When compared to neutron and x-ray diffraction techniques, PACBED is unique in its powerful capacity for atomic-scale characterization. This method is compatible with four-dimensional (4D)-STEM imaging with the advent of high dynamic range direct electron detectors [43–45], allowing for mapping of local phenomena at high resolution in both real and reciprocal space. This method can further extend to investigate structural origins of emergent physical properties at the local scale, in particular in the vicinity of interfaces and defects in quantum materials.

This work is supported by Center for Emergent Materials at the Ohio State University, a National Science Foundation Materials Research Science and Engineering Center (Grant No. DMR-1420451). Partial support is provided by the Center for Electron Microscopy and Analysis at the Ohio State University, as well as by an allocation of computing time from the Ohio Supercomputer Center.

[1] M. Coey, Nature **430**, 155 (2004).
[2] E. J. Moon, P. V. Balachandran, B. J. Kirby, D. J. Keavney, R. J. Sichel-Tissot, C. M. Schleputz, E. Karapetrova, X. M. Cheng, J. M. Rondinelli, and S. J. May, Nano Lett. **14**, 2509 (2014).
[3] Y. Tokura and N. Nagaosa, Science **288**, 462 (2000).
[4] J. B. Goodenough, Phys. Rev. **100**, 564 (1955).
[5] J. Rodriguez-Carvajal, M. Hennion, F. Moussa, A. H. Moudden, L. Pinsard, and A. Revcolevschi, Phys. Rev. B **57**, R3189 (1998).
[6] M. W. Lufaso and P. M. Woodward, Acta Crystallogr., Sect. B **60**, 10 (2004).
[7] J. B. Goodenough and J. S. Zhou, J. Mater. Chem. **17**, 2394 (2007).
[8] J. H. Song, J. H. Park, K.-B. Lee, J. M. Lee, and Y. H. Jeong, Phys. Rev. B **66**, 020407(R) (2002).
[9] S. J. May, J.-W. Kim, J. M. Rondinelli, E. Karapetrova, N. A. Spaldin, A. Bhattacharya, and P. J. Ryan, Phys. Rev. B **82**, 014110 (2010).
[10] J. M. Rondinelli, S. J. May, and J. W. Freeland, MRS Bull. **37**, 261 (2012).
[11] G. Sanchez-Santolino, M. Cabero, M. Varela, J. Garcia-Barriocanal, C. Leon, S. J. Pennycook, and J. Santamaria, Microsc. Microanal. **20**, 825 (2014).
[12] R. Erni, M. D. Rossell, C. Kisielowski, and U. Dahmen, Phys. Rev. Lett. **102**, 096101 (2009).
[13] Y. Jiang, Z. Chen, Y. Han, P. Deb, H. Gao, S. Xie, P. Purohit, M. W. Tate, J. Park, S. M. Gruner *et al.*, Nature **559**, 343 (2018).
[14] A. Y. Borisevich, H. J. Chang, M. Huijben, M. P. Oxley, S. Okamoto, M. K. Niranjan, J. D. Burton, E. Y. Tsymbal, Y. H. Chu, P. Yu *et al.*, Phys. Rev. Lett. **105**, 087204 (2010).
[15] R. Aso, D. Kan, Y. Shimakawa, and H. Kurata, Sci. Rep. **3**, 2214 (2013).
[16] N. Shibata, T. Seki, G. Sánchez-Santolino, S. D. Findlay, Y. Kohno, T. Matsumoto, R. Ishikawa, and Y. Ikuhara, Nat. Commun. **8**, 15631 (2017).
[17] A. Borisevich, O. S. Ovchinnikov, H. J. Chang, M. P. Oxley, P. Yu, J. Seidel, E. A. Eliseev, A. N. Morozovska, R. Ramesh, S. J. Pennycook *et al.*, ACS Nano **4**, 6071 (2010).
[18] Q. He, R. Ishikawa, A. R. Lupini, L. Qiao, E. J. Moon, O. Ovchinnikov, S. J. May, M. D. Biegalski, and A. Y. Borisevich, ACSs Nano **9**, 8412 (2015).
[19] A. B. Yankovich, B. Berkels, W. Dahmen, P. Binev, S. I. Sanchez, S. A. Bradley, A. Li, I. Szlufarska, and P. M. Voyles, Nat. Commun. **5**, 4155 (2014).
[20] C. Ophus, J. Ciston, and C. T. Nelson, Ultramicroscopy **162**, 1 (2016).
[21] A. Glazer, Acta Crystallogr., Sect. B **28**, 3384 (1972).
[22] M. W. Lufaso, P. W. Barnes, and P. M. Woodward, Acta Crystallogr., Sect. B: Struct. Sci. **62**, 397 (2006).
[23] S. Ismail-Beigi, F. J. Walker, A. S. Disa, K. M. Rabe, and C. H. Ahn, Nat. Rev. Mater. **2**, 17060 (2017).
[24] D. Bird and M. Saunders, Ultramicroscopy **45**, 241 (1992).
[25] K. Tsuda and M. Tanaka, Acta Crystallogr. Sect. A: Found. Crystallogr. **55**, 939 (1999).
[26] J. Zuo, M. Kim, M. O'Keeffe, and J. Spence, Nature **401**, 49 (1999).
[27] M. A. Spackman, B. Jiang, T. L. Groy, H. He, A. E. Whitten, and J. C. H. Spence, Phys. Rev. Lett. **95**, 085502 (2005).
[28] K. Tsuda, Y. Ogata, K. Takagi, T. Hashimoto, and M. Tanaka, Acta Crystallogr., Sect. A: Found. Crystallogr. **58**, 514 (2002).
[29] J. M. LeBeau, S. D. Findlay, L. J. Allen, and S. Stemmer, Ultramicroscopy **110**, 118 (2010).
[30] J. Hwang, J. Y. Zhang, J. Son, and S. Stemmer, Appl. Phys. Lett. **100**, 191909 (2012).
[31] J. Hwang, J. Son, J. Y. Zhang, A. Janotti, C. G. Van de Walle, and S. Stemmer, Phys. Rev. B **87**, 060101(R) (2013).
[32] J. Pollock, M. Weyland, D. Taplin, L. Allen, and S. Findlay, Ultramicroscopy **181**, 86 (2017).
[33] R. Bjørge, C. Dwyer, M. Weyland, P. Nakashima, C. Marioara, S. Andersen, J. Etheridge, and R. Holmestad, Acta Mater. **60**, 3239 (2012).
[34] J. M. LeBeau, A. J. D'Alfonso, N. J. Wright, L. J. Allen, and S. Stemmer, Appl. Phys. Lett. **98**, 052904 (2011).
[35] G. Trimarchi and N. Binggeli, Phys. Rev. B **71**, 035101 (2005).
[36] B. D. Forbes, A. V. Martin, S. D. Findlay, A. J. D'Alfonso, and L. J. Allen, Phys. Rev. B **82**, 104103 (2010).
[37] H. Yoshioka, J. Phys. Soc. Jpn. **12**, 618 (1957).
[38] L. J. Allen and S. Findlay, Ultramicroscopy **151**, 11 (2015).
[39] Q. Huang, A. Santoro, J. W. Lynn, R. W. Erwin, J. A. Borchers, J. L. Peng, and R. L. Greene, Phys. Rev. B **55**, 14987 (1997).
[40] E. J. Kirkland, *Advanced Computing in Electron Microscopy* (Springer Science & Business Media, Berlin, 2010).

[41] J.-M. Zuo, Mater. Trans., JIM **39**, 938 (1998).
[42] J. Alonso, M. Martinez-Lope, M. Casais, and M. Fernandez-Diaz, Inorg. Chem. **39**, 917 (2000).
[43] R. Ballabriga, M. Campbell, E. Heijne, X. Llopart, L. Tlustos, and W. Wong, Nucl. Instrum. Methods Phys. Res., Sect. A **633**, S15 (2011).
[44] M. W. Tate, P. Purohit, D. Chamberlain, K. X. Nguyen, R. Hovden, C. S. Chang, P. Deb, E. Turgut, J. T. Heron, D. G. Schlom *et al.*, Microsc. Microanal. **22**, 237 (2016).
[45] I. J. Johnson, K. C. Bustillo, J. Ciston, B. R. Draney, P. Ercius, E. Fong, A. Goldschmidt, J. M. Joseph, J. R. Lee, A. M. Minor *et al.*, Microsc. Microanal. **24**, 166 (2018).